Intermediate honeycomb ordering to trigger oxygen redox chemistry in layered battery electrode

Benoit Mortemard de Boisse[1,2], Guandong Liu[1], Jiangtao Ma[1], Shin-ichi Nishimura[1,2], Sai-Cheong Chung[1,2], Hisao Kiuchi[3], Yoshihisa Harada[4,5], Jun Kikkawa[6], Yoshio Kobayashi[7,8], Masashi Okubo[1,2] & Atsuo Yamada[1,2]

Sodium-ion batteries are attractive energy storage media owing to the abundance of sodium, but the low capacities of available cathode materials make them impractical. Sodium-excess metal oxides Na_2MO_3 (M: transition metal) are appealing cathode materials that may realize large capacities through additional oxygen redox reaction. However, the general strategies for enhancing the capacity of Na_2MO_3 are poorly established. Here using two polymorphs of Na_2RuO_3, we demonstrate the critical role of honeycomb-type cation ordering in Na_2MO_3. Ordered Na_2RuO_3 with honeycomb-ordered $[Na_{1/3}Ru_{2/3}]O_2$ slabs delivers a capacity of $180\,mAh\,g^{-1}$ (1.3-electron reaction), whereas disordered Na_2RuO_3 only delivers $135\,mAh\,g^{-1}$ (1.0-electron reaction). We clarify that the large extra capacity of ordered Na_2RuO_3 is enabled by a spontaneously ordered intermediate Na_1RuO_3 phase with ilmenite O1 structure, which induces frontier orbital reorganization to trigger the oxygen redox reaction, unveiling a general requisite for the stable oxygen redox reaction in high-capacity Na_2MO_3 cathodes.

[1] Department of Chemical System Engineering, School of Engineering, The University of Tokyo, Hongo 7-3-1, Bunkyo-ku, Tokyo 113-8656, Japan. [2] Elements Strategy Initiative for Catalysts & Batteries (ESICB), Kyoto University, Nishikyo-ku, Kyoto 615-8245, Japan. [3] Department of Applied Chemistry, School of Engineering, The University of Tokyo, Bunkyo-ku, Tokyo 113-8656, Japan. [4] Institute for Solid State Physics, The University of Tokyo, Kashiwa, Chiba 277-8581, Japan. [5] Synchrotron Radiation Research Organization, The University of Tokyo, Tatsuno, Hyogo 679-5165, Japan. [6] Advanced Key Technologies Division, National Institute for Materials Science, Tsukuba, Ibaraki 305-0044, Japan. [7] Department of Engineering Science, The University of Electro-Communications, Chofu, Tokyo 182-8585, Japan. [8] RIKEN Nishina Center for Accelerator-Based Science, RIKEN, Wako, Saitame 351-0198, Japan. Correspondence and requests for materials should be addressed to A.Y. (email: yamada@chemsys.t.u-tokyo.ac.jp).

Li-ion batteries power almost all of today's portable electronics and their ability to store energy is increasingly important for large-scale applications such as electric vehicles and power grids. However, Li resources are limited and unevenly distributed geographically; hence, alternatives need to be found. Na-ion batteries have garnered great attention as candidates for large-scale applications owing to the abundance and low cost of sodium. Accordingly, Na-ion (de)intercalation compounds have been explored intensively[1–8].

Among the various positive electrode materials that have been investigated, layered transition metal oxides $NaMO_2$ (M = transition metal) are considered to be the most promising[3,9–13], in part owing to their large theoretical capacities and the simple analogies from the successful application of $LiMO_2$ in Li-ion battery systems. However, the stably cyclable capacity of $NaMO_2$ is too small for practical use because deintercalation of a large amount of Na ions from the Na layer between the MO_2 slabs usually causes irreversible structural changes[14,15].

Replacing M atoms in the MO_2 slab with Na (for example, $Na[Na_{1/3}M_{2/3}]O_2$ or Na_2MO_3) is an appealing strategy to suppress these structural changes over a wider compositional range. The $[Na_{1/3}M_{2/3}]O_2$ slabs supply additional Na ions, thereby increasing the reversible capacity while suppressing the over-deintercalation of Na ions from the Na layer. This '$A_{2-x}MO_3$' strategy has already been adopted in many lithium systems such as Li_2MnO_3–$LiMO_2$ and Li_2RuO_3, in which enhanced capacities exceeding a M^{4+}/M^{3+} one-electron reaction have been achieved through additional oxygen redox contribution[16–18].

In our previous work, we applied this strategy to sodium systems, using a model compound, Na_2RuO_3 ($Na[Na_{1/3}Ru_{2/3}]O_2$)[19]. However, despite the presence of $[Na_{1/3}Ru_{2/3}]O_2$ slabs, Na_2RuO_3 delivered a modest capacity of $135\,mAh\,g^{-1}$, limited to the Ru^{5+}/Ru^{4+} one-electron reaction. In contrast, Rozier et al.[20] very recently reported that Na_2RuO_3 can deliver a capacity greatly exceeding that of the Ru^{5+}/Ru^{4+} one-electron reaction. At present, the discrepancy between the reported electrochemical properties is an open question. More generally, the requisite conditions for successful application of the '$A_{2-x}MO_3$' strategy for large-capacity sodium systems are poorly understood.

Here we demonstrate that a highly stabilized intermediate phase with honeycomb-type cation ordering in the $[Na_{1/3}M_{2/3}]O_2$ slab is critical for the effective use of the '$A_{2-x}MO_3$' strategy, by comparing two polymorphs of Na_2RuO_3; namely, 'ordered' Na_2RuO_3 with honeycomb-ordered $[Na_{1/3}M_{2/3}]O_2$ slabs and 'disordered' Na_2RuO_3 with randomly distributed $[Na_{1/3}M_{2/3}]O_2$ slabs (Fig. 1).

Results

Structural characterization of Na_2RuO_3. Ordered Na_2RuO_3 (hereafter denoted O-Na_2RuO_3) was synthesized by a thermal decomposition method, in which Na_2RuO_4 was annealed at 850 °C for 48 h under an Ar atmosphere[21]. Disordered Na_2RuO_3 (hereafter denoted D-Na_2RuO_3) was synthesized for comparison according to our previously reported procedure[19]. The ^{99}Ru Mössbauer spectra of both compounds (insets in Fig. 2a,b) show a singlet absorption peak with an isomer shift around $-0.3\,mm\,s^{-1}$, which is a typical value for Ru^{4+} (for example, $-0.25\,mm\,s^{-1}$ for $Y_2Ru_2O_7$ and $-0.33\,mm\,s^{-1}$ for $SrRuO_3$)[22], suggesting successful formation of stoichiometric Na_2RuO_3 compositions from both syntheses. The synchrotron X-ray diffraction (XRD) pattern of D-Na_2RuO_3 (Fig. 2a) is fully indexed to the O3 structure ($R\bar{3}m$ space group, $a = 3.0969(3)$ Å and $c = 15.970(2)$ Å); all diffraction peaks are well-fitted by Rietveld refinement with a structural model in which Na and Ru
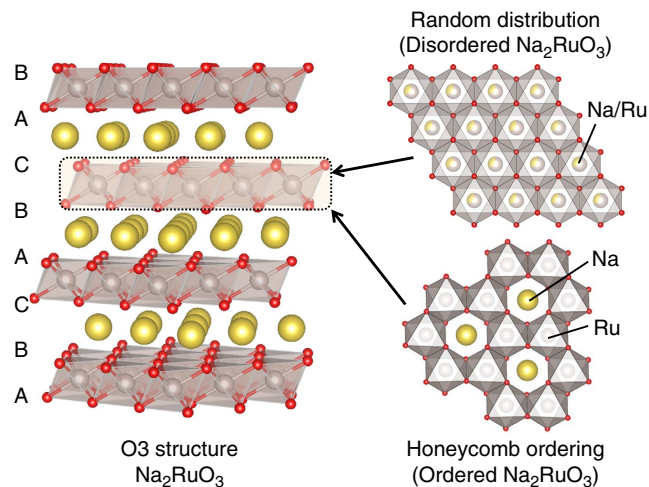

Figure 1 | Structure of ordered and disordered Na_2RuO_3. Oxide ions (red) stack in the manner of ABCABC while both Na (yellow) and Ru (grey) occupy octahedral sites for both Na_2RuO_3. Ordered Na_2RuO_3 has the honeycomb-type cation ordering in the $[Na_{1/3}Ru_{2/3}]O_2$ slab. Disordered Na_2RuO_3 has the randomly distributed $[Na_{1/3}Ru_{2/3}]O_2$ slab.

are randomly distributed in the $[Na_{1/3}Ru_{2/3}]O_2$ slabs (Fig. 1 and Supplementary Table 1). Na in the Na layer occupies octahedral sites and the oxide ions are stacked in an ABCABC arrangement (O3 structure)[23]. The selected area electron diffraction (SAED) pattern along the $[001]_{hex}$ zone axis (Fig. 2c) shows diffraction spots fully indexed by the $R\bar{3}m$ model with disordered $[Na_{1/3}Ru_{2/3}]O_2$ slabs.

The synchrotron XRD pattern of O-Na_2RuO_3 (Fig. 2b and Supplementary Table 1) is similar to that of D-Na_2RuO_3 and is almost fitted by Rietveld refinement in the $R\bar{3}m$ space group ($a = 3.1195(5)$ Å and $c = 15.989(4)$ Å) assuming disordered $[Na_{1/3}Ru_{2/3}]O_2$ slabs. However, diffuse scatterings remain, as highlighted by the black arrows in Fig. 2b. Similar characteristics have been reported for many A_2MO_3 (A = Li, Na and M = transition metal(s)) materials, and usually arise from honeycomb ordering in the MO_2 slabs[16,17,20]. Indeed, the SAED pattern along the $[001]_{hex}$ zone axis (Fig. 2d) shows many extra diffraction spots, which are not predicted using the standard $R\bar{3}m$ model with disordered $[Na_{1/3}Ru_{2/3}]O_2$ slabs. These spots can be indexed to a $\sqrt{3}a_{hex} \times \sqrt{3}b_{hex}$ supercell arising from the honeycomb ordering of Na and Ru in the $[Na_{1/3}Ru_{2/3}]O_2$ slabs (Fig. 1). In contrast, the SAED pattern along the $[110]_{hex}$ zone axis (Fig. 2e) shows extra streaks along $[001]_{hex}$. This feature is characteristic of stacking faults in honeycomb-ordered $[A_{1/3}M_{2/3}]O_2$ slabs along the c_{hex} direction, explaining the diffusive nature of the superstructure reflections in Fig. 2b (ref. 24).

Electrochemical properties of Na_2RuO_3. Having demonstrated the differences between O- and D-Na_2RuO_3 in terms of the in-plane ordering and stacking sequences of the $[Na_{1/3}Ru_{2/3}]O_2$ slabs, the Na^+ (de)intercalation properties of both materials were studied to clarify the influence of the honeycomb ordering. Figure 3a,b shows the charge–discharge curves measured between 1.5 and 4.0 V versus Na/Na^+ at $30\,mA\,g^{-1}$ (a rate of ~C/5). Here charging is an anodic process (Na deintercalation) and discharging is a cathodic process (Na intercalation). D-Na_2RuO_3 (Fig. 3a) delivers a reversible capacity of $135\,mAh\,g^{-1}$, corresponding to (de)intercalation of 1.0 Na^+, which is consistent with our previous report[19]. In contrast, the reversible capacity of
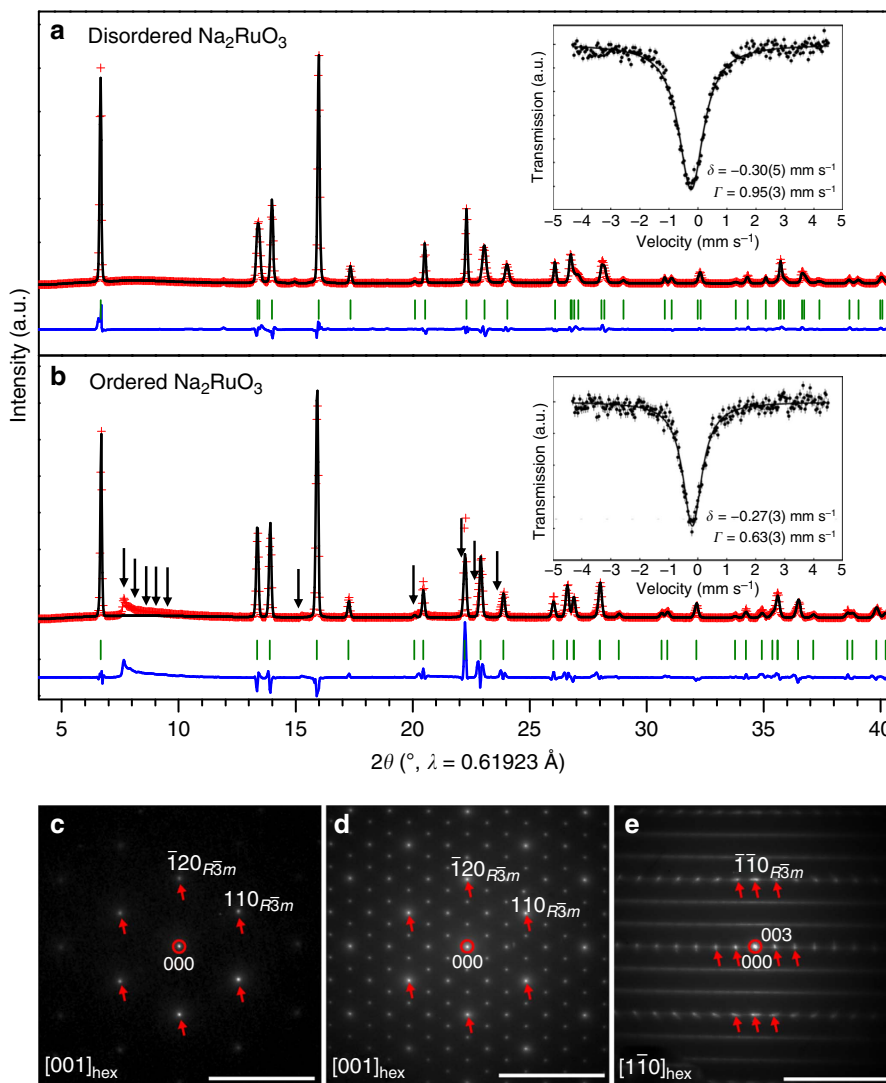
Figure 2 | Structural characterization of disordered and ordered Na$_2$RuO$_3$. Observed and calculated (Rietveld method) synchrotron X-ray diffraction patterns for (**a**) disordered and (**b**) ordered Na$_2$RuO$_3$. Red crosses: experimental, black line: calculated, blue line: difference and green bars: Bragg positions. The black arrows in **b** indicate the superstructure peaks that were not considered for the refinement. Insets of **a**,**b** correspond to the ^{99}Ru Mössbauer spectra recorded at 4.2 K for both pristine materials. Vertical error bars represent 1σ s.d. of counting statistics. Selected area electron diffraction (SAED) patterns in the (**c**) [001]$_{hex}$ zone axes of disordered Na$_2$RuO$_3$, and in the (**d**) [001]$_{hex}$ and (**e**) [1$\bar{1}$0]$_{hex}$ zone axes of ordered Na$_2$RuO$_3$. The red circles and arrows, respectively, indicate the central and fundamental diffraction spots, which are common to disordered Na$_2$RuO$_3$. Un-marked diffraction spots in between correspond to superstructure peaks. Scale bars, 10 nm^{-1}.

O-Na$_2$RuO$_3$ exceeds 180 mAh g^{-1}, indicating reversible (de)intercalation of 1.3 Na$^+$, beyond a Ru^{5+}/Ru^{4+} one-electron redox process. This behaviour is in agreement with that of Na$_2$RuO$_3$ reported by Rozier et al.[20]. Importantly, the voltage profile of O-Na$_2$RuO$_3$ significantly differs from the S-shaped voltage profile of D-Na$_2$RuO$_3$. O-Na$_x$RuO$_3$ (0.7 ≤ x ≤ 2) exhibits a staircase-like charge profile with a first voltage plateau around 2.5 V for 1.0 ≤ x ≤ 2.0 and a second voltage plateau around 3.6 V for 0.7 ≤ x ≤ 1.0; the second voltage plateau is related to the extra capacity of O-Na$_2$RuO$_3$, which exceeds that of the Ru^{5+}/Ru^{4+} one-electron reaction. Although the plateau at 3.6 V shows gradual narrowing with repeating the cycles presumably due to slight loss of the crystallinity (Supplementary Fig. 1a,b), O-Na$_2$RuO$_3$ shows excellent capacity retention of 160 mAh g^{-1} after 50 cycles (Fig. 3c), which indicates the remarkable stability of the redox processes that contribute to the increased capacity. Indeed, the voltage plateau

around 3.6 V is clearly observed for every charge process, suggesting occurrence of the accumulative oxygen redox reaction (Supplementary Fig. 1c,d)[18]. Therefore, the available capacity significantly exceeds one-electron redox reaction for O-Na$_2$RuO$_3$ even after 50 cycles. It is surprising that the in-plane honeycomb-type cation ordering in O-Na$_2$RuO$_3$ is solely responsible for the drastic changes in the electrochemical properties that results in 30% higher capacity. To the best of our knowledge, this is the first demonstration of the critical role of honeycomb-type cation ordering in [A$_{1/3}$M$_{2/3}$]O$_2$ slabs in determining the primary electrochemical properties.

Structural change during (de)sodiation. To clarify the reaction mechanisms in Na$_2$RuO$_3$, we studied the structural changes of D-Na$_2$RuO$_3$ and O-Na$_2$RuO$_3$ during cycling (Fig. 4a–d). As reported previously[19] and further supported by ex situ XRD
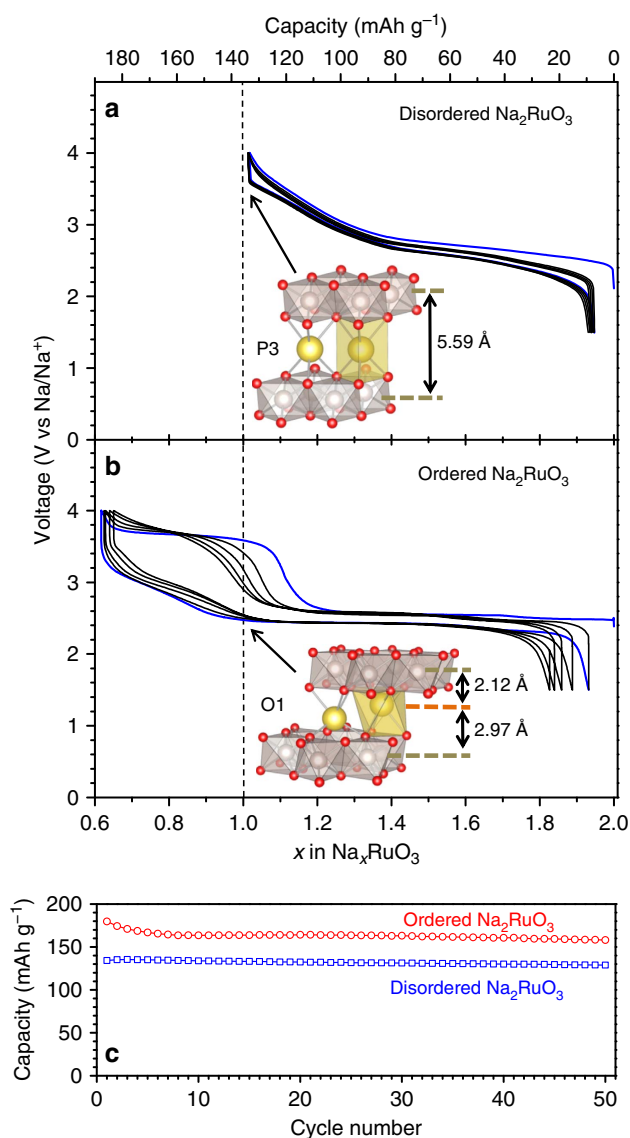
Figure 3 | Electrochemical properties of disordered and ordered Na₂RuO₃. Galvanostatic cycling curves recorded at 30 mA g⁻¹ for (**a**) disordered and (**b**) ordered Na₂RuO₃ with the first cycle highlighted in blue. Insets show the coordination environment of Na at $x = 1.0$ for each phase. (**c**) Capacity retentions for (blue squares) disordered and (red circles) ordered Na₂RuO₃.

patterns (Supplementary Fig. 2), D-Na$_x$RuO₃ undergoes a structural change from O3 to P3 (with Na in prismatic sites owing to the ABBCCA oxide-ion stacking) on charging[23]. This O3→P3 transition is commonly observed in O3-NaMO₂ materials through gliding of the [Na$_{1/3}$Ru$_{2/3}$]O₂ slabs from ABCABC (O3) to ABBCCA (P3) stacking[9,25]. The synchrotron XRD pattern of the charged state (D-Na₁RuO₃; Supplementary Fig. 3 and Supplementary Table 2) is fully fitted by the Rietveld refinement assuming a P3 structure ($R\bar{3}m$ space group, $a = 2.927(2)$ Å and $c = 16.774(12)$ Å), in which Na ions in the Na layer are located in prismatic sites (inset in Fig. 3a). The interlayer distance is significantly increased from 5.323(1) Å ($x = 2$) to 5.591(4) Å ($x = 1$) because of the high aspect ratio of the prismatic Na sites in the P3 structure (Fig. 4a).

It should be emphasized that O-Na₂RuO₃ exhibits a completely different structural evolution from D-Na₂RuO₃ on charging. The

in situ and *ex situ* XRD patterns of O-Na₂RuO₃ (Supplementary Figs 4 and 5) at the first plateau show that an intermediate phase 'X' with an unknown structure (presumably a P-type phase based on the interlayer distance of around 5.5 Å) appears during the initial stages of the desodiation, and that the O3 phase is eventually transformed to a new phase at $x = 1$ with an extremely short interlayer distance of around 5.2 Å (Fig. 4a). These complex equilibria among the O3, X and O1 phases are responsible for the long voltage plateau observed in the $1 \leq x \leq 2$ composition range of O-Na$_x$RuO₃. On charging, the diffuse scatterings of the superstructure gradually disappear, while new, well-resolved peaks appear (Fig. 4d). The well-resolved character of the new superstructure reflections suggest that the disordered stacking of the honeycomb lattice is spontaneously adjusted towards the ordered state during electrochemical desodiation. The Rietveld refinement and SAED pattern of O-Na₁RuO₃ (Fig. 4b,c and Supplementary Tables 2 and 3) confirm that the [Na$_{1/3}$Ru$_{2/3}$]O₂ layers maintain the original honeycomb-type in-plane ordering. As shown in Fig. 4b, the ABCABC stacking sequence of oxygen is transformed to an ABAB sequence, in which Na in the Na layer occupies octahedral sites (O1 structure; inset in Fig. 3b). This ordered structure is isomorphic with the ilmenite FeTiO₃-type structure[26].

In the refined structure of O-Na₁RuO₃ ($R\bar{3}$ space group, $a = 5.2492(1)$ Å and $c = 15.6201(6)$ Å), the Na site in the [Na$_{1/3}$Ru$_{2/3}$]O₂ slabs is vacant, which means Na was extracted from the [Na$_{1/3}$Ru$_{2/3}$]O₂ slabs prior to the Na layers. In this very unique, stable intermediate ilmenite-type Na₁RuO₃, all NaO₆ octahedra in the Na layer share faces with a RuO₆ octahedron and a '□O₆' octahedron of the adjacent [□$_{1/3}$Ru$_{2/3}$]O₂ slabs (□: Na vacancy). As shown in Fig. 4a, the interlayer distance of O-Na₁RuO₃ (5.2067(2) Å) is much shorter than that of D-Na₁RuO₃ (5.591(4) Å) as a result of substantial displacement of Na in the Na layer towards □O₆ octahedra by Coulombic attraction (Fig. 4b). Importantly, the RuO₆ octahedron is strongly distorted: the shortest neighbouring O–O distance is 2.580(4) Å, whereas the longest is 3.080(6) Å (Fig. 5 and Supplementary Table 3).

The ilmenite structure of O-Na₁RuO₃ is stabilized by the following mechanisms: (1) the ordered Na arrangement minimizes Na⁺–Na⁺ repulsion; (2) the Na vacancy □ in the [□$_{1/3}$Ru$_{2/3}$]O₂ slab strongly attracts Na ions in the face-sharing octahedra in adjacent Na layers; (3) the ordered and displaced arrangement of Na ions minimizes Ru⁵⁺–Na⁺ repulsive interactions; and (4) the cooperative distortion of the RuO₆ octahedra can minimize the total strain energy in the ordered honeycomb lattice. All these mechanisms lead to the formation of the ilmenite phase with well-ordered stacking of the honeycomb lattices.

On discharge, *in situ* XRD patterns (Supplementary Fig. 4) prove that the phase transformation is almost reversible except for a small asymmetry, that is, the appearance of the X phase only at charge. Presumably, this parasitic asymmetric behaviour is observed under non-equilibrium conditions such as the microscale heterogeneity.

Electronic structure of Na₂₋ₓRuO₃. After the O3→O1 transition, O-Na₂RuO₃ delivers additional capacity, exceeding that of the Ru⁵⁺/Ru⁴⁺ one-electron reaction at the higher voltage plateau of around 3.7 V. To clarify the overall redox mechanism in O-Na₂RuO₃, we conducted Ru L_3-edge and oxygen K-edge X-ray absorption spectroscopy (XAS) in the partial fluorescence yield mode at various charge depths (Fig. 6, Supplementary Figs 6 and 7). The Ru L_3-edge XAS directly probes the 4d orbitals through the Laporte-allowed 2p→4d transition[27]. Furthermore, because the O 2p orbital strongly hybridizes with the Ru 4d
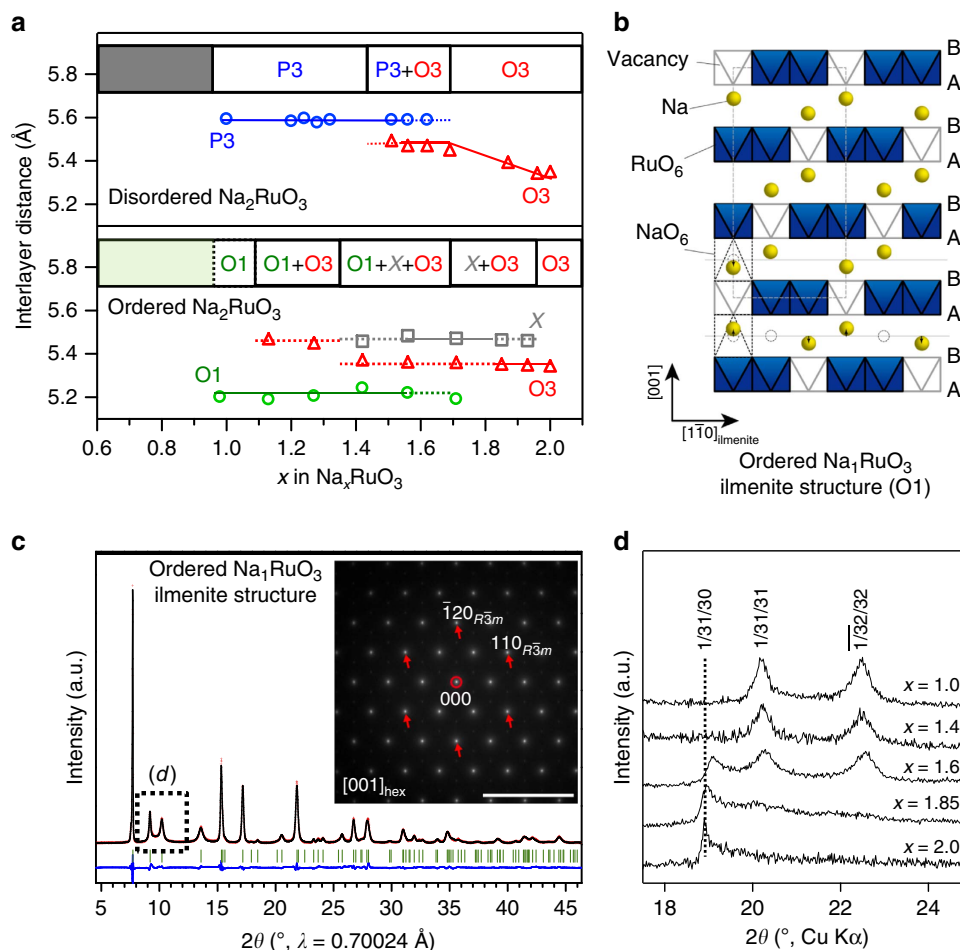
Figure 4 | Structural changes of disordered and ordered Na_2RuO_3 during charge. (**a**) Interlayer distance of the different phases involved on desodiation as a function of x in disordered and ordered Na_xRuO_3. (**b**) Crystal structure of ilmenite-type Na_1RuO_3. All Na ions displace cooperatively towards Na vacancies in the honeycomb planes. (**c**) Observed and calculated (Rietveld method) synchrotron X-ray diffraction patterns for ordered Na_1RuO_3. Red crosses: experimental, black line: calculated, blue line: difference and green bars: Bragg positions. The inset shows the selected area electron diffraction (SAED) pattern for ilmenite-type Na_1RuO_3. Scale bar, 10 nm^{-1} (**d**) *Ex situ* XRD patterns showing the evolution of the superstructure peaks for ordered Na_xRuO_3 on charge.

orbital, oxygen K-edge XAS can be used to monitor the hole created on the O 2p and Ru 4d orbitals on charging[28]. Note that the probing depth of the partial fluorescence yield mode is about 100 nm; hence, the spectra are bulk sensitive[29].

The Ru L_3-edge spectrum for pristine O-Na_2RuO_3 ($t_{2g}^4 e_g^0$, neglecting the trigonal distortion of Ru for clarity), Fig. 6b, shows two absorption peaks corresponding to the excitation from the $2p$ orbital to the unoccupied t_{2g} and e_g orbitals. The peak position for the $2p \rightarrow e_g$ absorption (2841.5 eV) is similar to that reported for Ru^{4+} (2841.6 eV) in $SrRuO_3$ and RuO_2 (ref. 27), confirming Ru^{4+} in pristine O-Na_2RuO_3. On charging to ilmenite-type Na_1RuO_3, two absorption peaks shift to higher energy. Since the peak position of the $2p \rightarrow e_g$ absorption for ilmenite-type Na_1RuO_3 (2,843 eV) agrees with that of Ru^{5+} in $Sr_4Ru_2O_9$ (ref. 27), oxidation from Ru^{4+} to Ru^{5+} occurs at the first potential plateau. However, further desodiation at the second plateau does not shift the $2p \rightarrow e_g$ absorption peak, suggesting no substantial change in the valence state of Ru.

The O K-edge spectrum of pristine O-Na_2RuO_3 ($t_{2g}^4 e_g^0$) shows a large peak at 534 eV, which is ascribed to the unoccupied hybridized orbital of O 2p–Na 3p, and its peak intensity simply reflects the amount of Na in the lattice[30]. The calculated density of states for O-Na_2RuO_3 (Fig. 7a) also indicates that the

O 2p–Na 3p hybridized orbital exists in this energy range. For the lower energy region that represents the redox reaction, the calculated oxygen K-edge spectrum agrees well with the spectra from 528 to 533 eV. Thus, the peaks around 529 eV and 532 eV can be ascribed to the unoccupied hybridized orbitals of O 2p–Ru t_{2g} and O 2p–Ru e_g, respectively[31,32]. At the voltage plateau of 2.5 V, desodiation diminishes the O 2p–Na 3p signal, whereas the peak intensity of O 2p–Ru t_{2g} (around 529 eV) increases on charging, indicating hole generation on the O 2p–Ru t_{2g} orbital. The increase in the peak intensity around 529 eV is also in good agreement with the calculated oxygen K-edge spectrum for ilmenite-type Na_1RuO_3.

On further charging at the second plateau (around 3.6 V), the peak intensity of the O 2p–Ru t_{2g} is almost constant, whereas the peak around 532 eV broadens as a result of the new absorption band emerging around 533 eV. This spectral change cannot be explained by $Ru^{5+} \rightarrow Ru^{6+}$ oxidation (hole generation on O 2p–Ru t_{2g}). One possible explanation is the formation of a new chemical bond involving oxygen. For example, formation of an O–O bond (that is, peroxo/superoxo-like groups O_2^{n-} $(1 \leq n \leq 3)$) has been proposed as the oxygen redox mechanism for many $Li_2(M,M')O_3$ cathode materials (M,M' = Fe, Ru, Sb, Sn or Ir)[18,33,34]. Here the hole generated by further
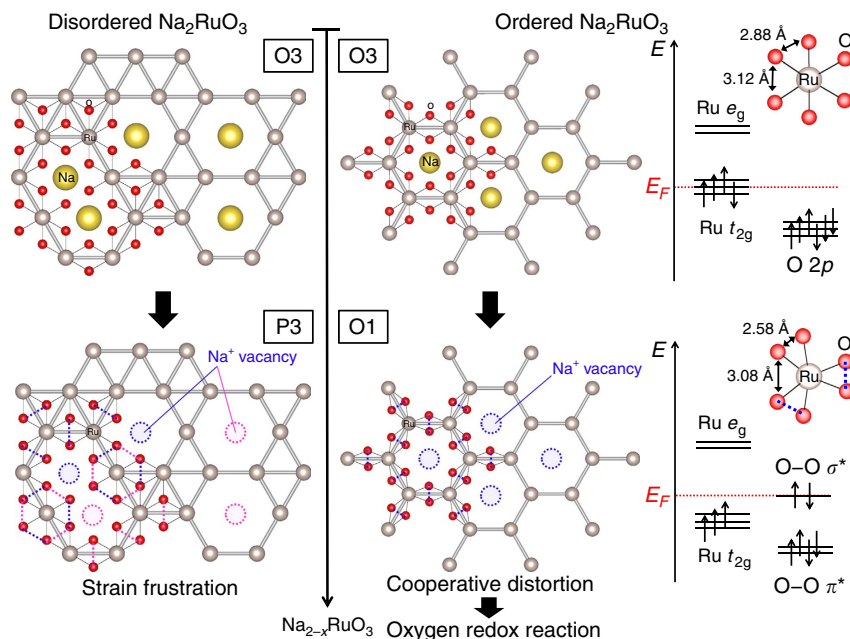
Figure 5 | Reaction mechanisms of disordered and ordered Na$_2$RuO$_3$. Schematic representation of the structural changes during charge–discharge for disordered Na$_2$RuO$_3$ and ordered Na$_2$RuO$_3$. Ordered Na$_2$RuO$_3$ can distort cooperatively to raise the energy level of the antibonding $\sigma^\star$ orbital of the O–O bond, leading to the oxygen redox reaction. Disordered Na$_1$RuO$_3$ cannot accommodate the RuO$_6$ distortion due to strain frustration, which prevents the oxygen redox reaction.

charging is stabilized on the antibonding $\sigma^\star$ orbital of the O–O bond which is covalently bonded to the transition metal. It should be noted that the ^{99}Ru Mössbauer spectrum of O–Na$_{0.62}$RuO$_3$ (Supplementary Fig. 8) shows absorption with an isomer shift of $\delta = +0.21\,\mathrm{mm\,s}^{-1}$, which is a typical value for Ru^{5+} ($+0.11\,\mathrm{mm\,s}^{-1}$ for Na$_3$RuO$_4$ and $+0.19\,\mathrm{mm\,s}^{-1}$ for Ca$_2$EuRuO$_6$)[22], supporting that no further Ru$^{5+} \to$ Ru^{6+} oxidation occurs.

On discharge, while the $2p \to t_{2g}$ and $2p \to e_g$ signals in the Ru L_3-edge spectra shift to the initial lower energy region, the O–O bond and O $2p$–Ru t_{2g} signals in the O K-edge spectra decrease reversibly (Supplementary Figs 6 and 7). Furthermore, although the diffraction peaks of the *ex situ* XRD pattern after cycling exhibit weak broadening due to the slight loss of the crystallinity, O-Na$_2$RuO$_3$ still shows characteristic diffuse scatterings similar to the pristine compound (Supplementary Fig. 1b), which suggests that the honeycomb-type in-plane ordering is maintained during the charge–discharge cycles for all Na compositions, where $0.7 \le x \le 2$. Importantly, this is the first simultaneous achievement of extra oxygen redox capacity and structural integrity leading to totally reversible oxygen participation. All other A_{2-x}MO$_3$-type electrodes suffer from severe structural rearrangement on the first charge and from lowering of the operating voltage during subsequent cycles[16,17,34–36]. This structural rearrangement occurs because M migrates from octahedral sites in the M layer to face-sharing tetrahedral sites in the adjacent A layer[35]. Presumably, this inter-site migration of Ru is suppressed in Na$_2$RuO$_3$ because of incompatibility of large Ru with the tetrahedral site. Furthermore, the interlayer O–O bond formation, which is predicted theoretically for delithiated Li$_2$MnO$_3$ to destabilize the oxygen redox reaction[37], should be inhibited by the large interlayer distance in Na$_x$RuO$_3$ (for example, $5.2-5.5$ Å for Na$_x$RuO$_3$ and $4.7-4.8$ Å for Li$_x$Ru$_{0.75}$Mn$_{0.25}$O$_3$)[36]. As shown in Supplementary Fig. 9, the initial Coulombic efficiency of O-Na$_2$RuO$_3$ is higher (95%) than that of other A_{2-x}MO$_3$ (for example, 70% for Li$_2$MnO$_3$ and 90% for Li$_2$RuO$_3$)[17,36,38,39].

Discussion

The critical role of honeycomb ordering in Na$_2$RuO$_3$ based on the aforementioned original observations is summarized in Fig. 5. The ordered $[\square_{1/3}\mathrm{Ru}_{2/3}]\mathrm{O}_2$ slabs in ilmenite O-Na$_1$RuO$_3$ accommodate the distortion of the RuO$_6$ octahedra cooperatively, whereby the shortest O–O distance is 2.580(4) Å. Because the short O–O distance raises the energy level of the antibonding $\sigma^\star$ orbital of the O–O bond to the Fermi level, the oxygen redox reaction is triggered. Indeed, the calculated density of states for ilmenite O-Na$_1$RuO$_3$ (Fig. 7b) shows that the occupied antibonding orbitals of the O–O bond exist near the Fermi level. The naturally derived scenario is that, once the hole is generated on the antibonding $\sigma^\star$ orbital of the O–O bond, the O–O distance becomes shorter[40]. This short distance leads to the higher energy level of the antibonding $\sigma^\star$ orbital of the oxygen–oxygen bond and an acceleration of the oxygen redox reaction. This hypothesis was recently reinforced by McCalla *et al.*[34]: scanning transmission electron microscopy and neutron diffraction on fully delithiated Li$_2$IrO$_3$ (Li$_{0.5}$IrO$_3$) determined the shorter O–O distance (2.45 Å) after the oxygen oxidation. However, as demonstrated in this work, the short O–O distance is required before the oxygen oxidation to achieve the extra capacity. For example, the disordered $[\mathrm{Na}_{1/3}\mathrm{Ru}_{2/3}]\mathrm{O}_2$ slabs in D-Na$_1$RuO$_3$ cannot accommodate the cooperative distortion of the RuO$_6$ octahedra owing to strain frustration. Thus, the O–O distances in D-Na$_1$RuO$_3$ are long enough (2.751(6) and 2.927(1) Å) so that the energy level of the antibonding $\sigma^\star$ orbital of the O–O bond is well below the Fermi level, which inhibits the extra oxygen redox process within the electrolyte stability window. Therefore, honeycomb-type cation ordering in the $[\mathrm{Na}_{1/3}\mathrm{M}_{2/3}]\mathrm{O}_2$ slab is a structural requisite condition to trigger the stable oxygen redox capacity in Na$_2$MO$_3$.

Finally, we mention the role of Ru in the oxygen redox reaction. Very recently, Saubanère *et al.*[37] theoretically demonstrated that the covalent bond between the peroxo-like $(\mathrm{O}_2)^{n-}$ $2p$ and Ru $4d$ orbitals in Li$_2$RuO$_3$ (reductive coupling
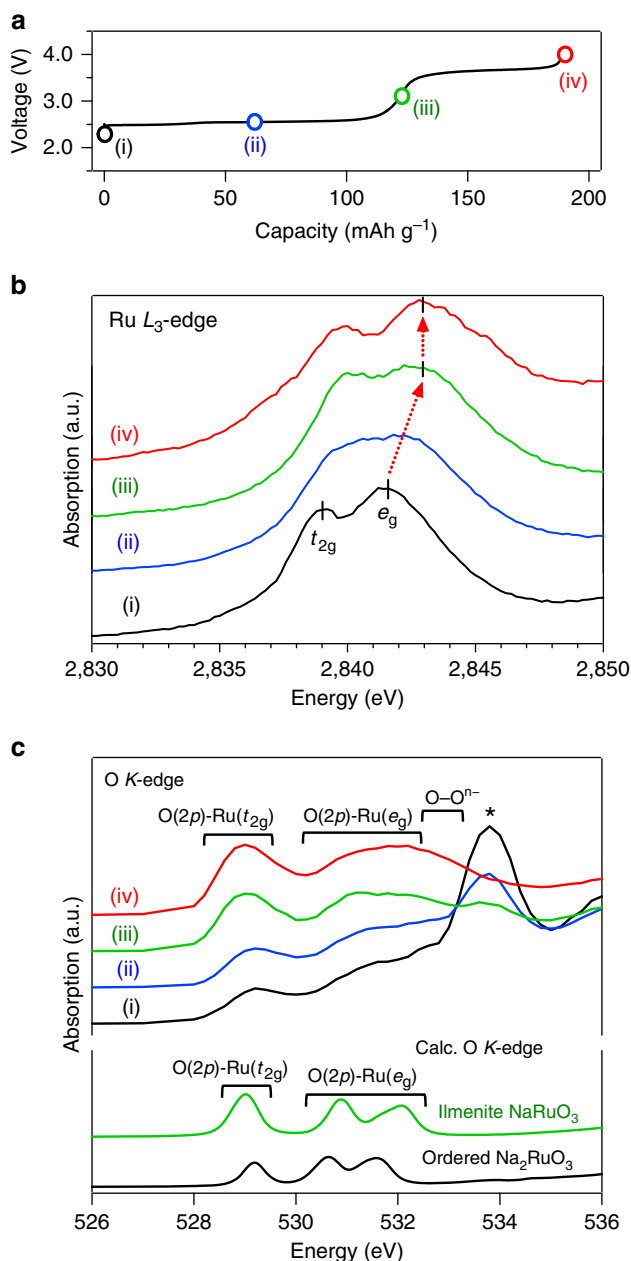
Figure 6 | Electronic structure changes of ordered Na₂RuO₃ upon charge.
(**a**) States of charge of the samples for X-ray absorption spectroscopy.
(**b**) Ruthenium L_3-edge and (**c**) oxygen K-edge X-ray absorption spectra for
various O-$Na_x RuO_3$ compositions: (i) $x = 2.0$ (black), (ii) $x = 1.5$ (blue),
(iii) $x = 1.0$ (green) and (iv) $x = 0.62$ (red). The asterisked peak
corresponds to O $2p$-Na $3p$. The calculated oxygen K-edge spectra for
ordered $Na_2 RuO_3$ (black) and ilmenite-type $NaRuO_3$ (green) are also
shown.

**Figure 7 | Calculated electronic structure of ordered Na₂RuO₃ upon
charge.** Calculated density of states (DOS) for ordered (**a**) O3-$Na_2 RuO_3$
and (**b**) ilmenite-type $Na_1 RuO_3$.

mechanism) is essential to facilitate the oxygen redox reaction
and to suppress the oxygen gas release, whereas the M(3d)-O(2p)
overlap is too small to enable this mechanism. For O-$Na_2 RuO_3$,
in addition to the stable structural nature inherent in the Na
system by suppressing both the inter-site Ru migration and the
interlayer O–O bond formation as discussed above, the similar
reductive coupling mechanism through the large orbital overlap
between the Ru $4d$ and O $2p$ orbitals should suppress the oxygen
gas release, which explains the high cycle stability of O-$Na_2 RuO_3$
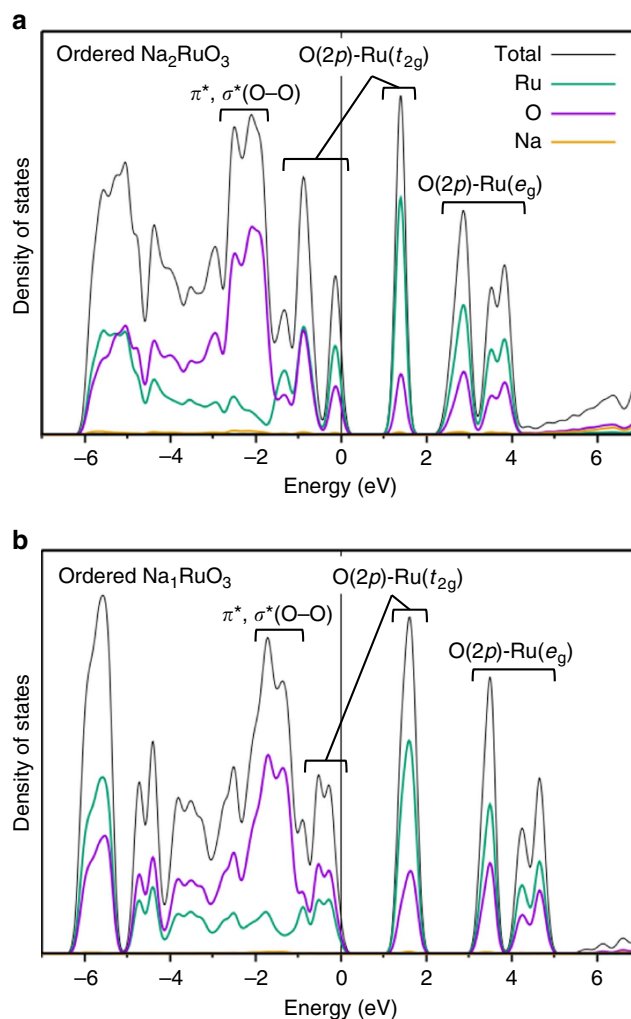compared with that of any other Li excess materials
(Supplementary Fig. 9).

In conclusion, the present work demonstrates the critical role
of honeycomb-type cation ordering in $Na_2 MO_3$ to achieve
enhanced reversible capacity based on the oxygen redox process.
In comparison to its disordered polymorph, O-$Na_2 RuO_3$ with in-
plane honeycomb ordering exhibits a significantly different
voltage profile, leading to a 30% extra capacity, spurred by the
electrochemically driven, further ordered intermediate, $NaRuO_3$,
which accommodates cooperative distortion of the RuO_6
octahedra. The short O–O distance in distorted RuO_6 induces
frontier orbital reorganization, triggering the oxygen redox
reaction.

To the best of our knowledge, this is the first report that
clarifies the underlying structural requirement to trigger the
oxygen redox reaction in $A_{2-x} MO_3$. By further exploiting the
compositional versatility of $A_2 MO_3$ while meeting this require-
ment, there is great potential to develop oxygen redox electrodes
for superior batteries. Considering the impact of the stable
intermediate on the overall electrode properties, the peculiar
phenomena and concepts demonstrated here may give general
implications for a deeper understanding and improved utilization
of intercalation materials.

Methods
Synthesis of Na₂RuO₃. Ordered $Na_2 RuO_3$ was synthesized by the thermal
decomposition method according to the literature where $Na_2 RuO_4$ was annealed at

850 °C for 48 h under Ar atmosphere[21]. Disordered Na_2RuO_3 was synthesized according to the procedure we previously reported[19]. The $NaHCO_3$ and RuO_2 precursors were calcined at 850 °C for 12 h under Ar atmosphere. Both compounds were handled in a globe box filled with Ar (dew point below -110 °C).

Materials characterization. Powder X-ray diffraction patterns were recorded on a Rigaku TTR-III diffractometer equipped with Cu $K\alpha$ radiation in 0.02° steps over the 2θ range of 10–80°. XRD patterns were measured at SPring-8 BL02B2 and Photon Factory BL-8B. The samples were handled without air exposure throughout the experiments. Rietveld refinements were carried out using Jana2006 (ref. 41) or TOPAS-Academic software. The profile of Na_1RuO_3 was better described using independent crystallite size for $00l$ reflections, Popa's sphere harmonics for $h0l$ and hkl reflections and different crystallite sizes for $(h0k) = 3n$ as implemented in TOPAS in order to take into account the stacking faults affecting part of the diffraction peaks. The crystal structures were drawn using VESTA[42]. SAED patterns were recorded using an electron microscope (HF-3000S; Hitachi Ltd.) operated at 300 kV and an imaging plate system (FDL-5000; Fujifilm). The camera length was calibrated with a Si crystal. ^{99}Ru Mössbauer spectroscopy was carried out with the ^{99}Rh source ($T_{1/2} = 15$ days), which was prepared by the $^{99}Ru(p,n)^{99}Rh$ reaction at the RIKEN AVF cyclotron. The $^{99}Ru(p,n)^{99}Rh$ reaction was conducted with a ^{99}Ru (95% enriched) target under 12 MeV proton irradiation. Both the source and the samples were cooled in liquid He during the measurements. The samples were transferred into the liquid He cryostat without air exposure. The Doppler velocity was calibrated by measuring a ^{57}Fe Mossbauer spectrum of α-Fe, and the zero velocity was determined by the isomer shift of Ru metal at 4.2 K.

Electrochemical measurement. For the electrochemical measurements, 80 wt% of Na_2RuO_3 was mixed with 10 wt% of acetylene black and 10 wt% of polyvinylidene in N-methyl pyrrolidone to make a slurry, which was then coated onto Al foil. The dried films were used as a cathode in the 2,032-type coin cells with Na metal as an anode. $NaPF_6$ (1 M) in ethylene carbonate/diethyl carbonate (1:1 v/v) was used as an electrolyte. The charge–discharge experiments were conducted at 30 mA g^{-1} between $1.5 - 4.0$ V versus Na/Na^+, within the electrolyte stability window.

Samples for *ex situ* characterization. The electrodes for *ex situ* XRD, XAS and ^{99}Ru Mossbauer spectroscopy were prepared as described above. O-Na_1RuO_3 samples for synchrotron XRD and TEM studies were prepared following the same method except that the positive electrode consisted in a pellet (Ø 10 mm, 50 mg) of O-Na_2RuO_3 that was sintered at 850 °C for 12 h. The batteries were then cycled to a designated voltage that was maintained for a few hours (Na_1RuO_3) or until a given current has been applied. After cycling, the batteries were introduced into an Ar-filled glovebox and the collected electrodes were washed three to five times with anhydrous dimethyl carbonate.

In situ XRD. *In situ* XRD (*operando* mode) was carried out using an *in situ* cell purchased from Rigaku on a D8 ADVANCE powder diffractometer equipped with Co $K\alpha$ radiation in 0.02° steps over the 2θ range of $17 - 25°$ (1.37 s per step, one pattern recorded every ≈ 12 min). The electrochemical part of the cell is similar to the one described above. The only exception lies in the preparation of the electrode whose slurry was coated on plastic films to be peeled off after drying. The current rate was C/20 (full (dis)charge theoretically achieved in 20 h), allowing us to record an XRD pattern every $\Delta x = 0.02$. Only selected patterns are shown in Supplementary Fig. 4 for clarity concerns. Electrochemistry was controlled and recorded using a Biologic VMP3.

X-ray absorption. O K-edge XAS was carried out at BL07LSU of SPring-8. The samples were transferred to a vacuum chamber without air exposure. Bulk-sensitive partial-fluorescence yield (PFY) mode was used for the O K-edge XAS. Energy resolution was approximately 100 meV. All the spectra were recorded using a silicon drift detector at room temperature. The spectra were normalized by the peak intensity at 532 eV, because the peak at 532 eV corresponding to O 2p-Ru e_g may not be affected by the redox of Ru^{5+}/Ru^{4+}. Ru L_3-edge XAS was carried out at BL27SU of SPring-8. The samples were transferred to a vacuum chamber without exposure to air. The spectra were recorded in the bulk-sensitive PFY mode using a silicon drift detector at room temperature.

Ab initio calculation. Spin-polarized DFT + U calculations were performed using the VASP code[43] with U_{eff} for Ru ranging from 0.5 to 4.5 eV. Van der Waals density functional optPBE[44] was employed. The plane-wave energy cut-off was set to 520 eV and the Brillouin zone integration was done in a k-point grid chosen to converge the energy to 10^{-4} eV. Atomic coordinates and lattice parameters were relaxed using conjugate gradient method until the maximum force on atoms is $< 2 \times 10^{-3}$ eV Å^{-1}. Initial geometry of Na_2RuO_3 in the $C2/m$ symmetry was taken from the literature[45] while the initial geometry for $NaRuO_3$ in the $R\bar{3}$ symmetry is from the present work. Antiferromagnetic ordering of spin on Ru was assumed, the pattern was set to be Néel type. The oxygen K-edge X-ray absorption

pattern was calculated by the WIEN2k code[46] employing the full potential linear augmented plane-wave method, dipole approximation to the golden rule for the transition probability was assumed.

References

1. Yabuuchi, N., Kubota, K., Dahbi, M. & Komaba, S. Research development on sodium-ion batteries. *Chem. Rev.* **114,** 11636–11682 (2014).
2. Kundu, D., Talaie, E., Duffort, V. & Nazar, L. F. The emerging chemistry of sodium ion batteries for electrochemical energy storage. *Angew. Chem. Int. Ed.* **54,** 3431–3448 (2015).
3. Yabuuchi, N. *et al.* P2-type $Na_x[Fe_{1/2}Mn_{1/2}]O_2$ made from earth-abundant elements for rechargeable Na batteries. *Nat. Mater.* **11,** 512–517 (2012).
4. Barpanda, P., Oyama, G., Nishimura, S., Chung, S. C. & Yamada, A. A 3.8 V Earth-abundant sodium battery electrode. *Nat. Commun.* **5,** 4358 (2014).
5. Billaud, J. *et al.* β-NaMnO₂: a high-performance cathode for sodium-ion batteries. *J. Am. Chem. Soc.* **136,** 17243–17248 (2014).
6. Wang, X. *et al.* Pseudocapacitance of MXene nanosheets for high-power sodium-ion hybrid capacitors. *Nat. Commun.* **6,** 6544 (2015).
7. Qian, J., Wu, X., Cao, Y., Ai, X. & Yang, H. High capacity and rate capability of amorphous phosphorous for sodium-ion batteries. *Angew. Chem. Int. Ed.* **52,** 4633–4636 (2013).
8. Wang, Y. *et al.* A zero-strain layered metal oxide as the negative electrode for long-life sodium-ion batteries. *Nat. Commun.* **3,** 2365 (2013).
9. Komaba, S. *et al.* Study on the reversible electrode reaction of $Na_{1-x}Ni_{0.5}Mn_{0.5}O_2$ for a rechargeable sodium-ion battery. *Inorg. Chem.* **51,** 6211–6220 (2012).
10. Wang, X., Liu, G., Iwao, T., Okubo, M. & Yamada, A. Role of ligand-to-metal charge transfer in O3-Type NaFeO₂-NaNiO₂ solid solution for enhanced electrochemical properties. *J. Phys. Chem. C* **118,** 2970–2976 (2014).
11. Mortemard de Boisse, B., Carlier, D., Guignard, M., Bourgeois, L. & Delmas, C. P2-$Na_xMn_{1/2}Fe_{1/2}O_2$ phase used as positive electrode in Na Batteries; structural changes induced by the electrochemical (De)intercalation process. *Inorg. Chem.* **53,** 11197–11205 (2014).
12. Li, X. *et al.* Direct visualization of the Jahn-Teller effect coupled to Na ordering in $Na_{5/8}MnO_2$. *Nat. Mater.* **13,** 586–592 (2014).
13. Billaud, J. *et al.* $Na_{0.67}Mn_{1-x}Mg_xO_2$ ($0 \le x \le 0.2$): a high capacity cathode for sodium-ion batteries. *Energy Environ. Sci.* **7,** 1387–1391 (2014).
14. Ma, X., Chen, H. & Ceder, G. Electrochemical properties of monoclinic NaMnO₂. *J. Electrochem. Soc.* **158,** A1307–A1312 (2015).
15. Yabuuchi, N., Yano, M., Yoshida, H., Kuze, S. & Komaba, S. Synthesis and electrode performance of O3-type NaFeO₂-NaNi₁/₂Mn₁/₂O₂ solid solution for rechargeable sodium batteries. *J. Electrochem. Soc.* **160,** A3131–A3137 (2013).
16. Thackeray, M. M., Johnson, C. S., Vaughey, J. T., Li, N. & Hackney, S. A. Advances in manganese-oxide 'composite' electrodes for lithium-ion batteries. *J. Mater. Chem.* **15,** 2257–2267 (2005).
17. Sathiya, M. *et al.* Reversible anionic redox chemistry in high-capacity layered-oxide electrodes. *Nat. Mater.* **12,** 827–835 (2013).
18. Sathiya, M. *et al.* Electron paramagnetic resonance imaging for real time monitoring of Li-ion batteries. *Nat. Commun.* **6,** 6276 (2015).
19. Tamaru, M., Wang, X., Okubo, M. & Yamada, A. Layered Na_2RuO_3 as a cathode material for Na-ion batteries. *Electrochem. Commun.* **33,** 23–26 (2013).
20. Rozier, P. *et al.* Anionic redox chemistry in Na-rich $Na_2Ru_{1-y}Sn_yO_3$ positive electrode materials for Na-ion batteries. *Electrochem. Commun.* **53,** 29–32 (2015).
21. Mogare, K. M., Friese, K., Klein, W. & Jansen, M. Synthesis and crystal structures of two sodium ruthenate: Na_2RuO_4 and Na_2RuO_3. *Z. Anorg. Chem.* **630,** 547–552 (2004).
22. Gütlich, P., Bill, E. & Trautwein, A. X. in *Mössbauer Spectroscopy and Transition Metal Chemistry* (Springer-Verlag, 2011).
23. Delmas, C., Fouassier, C. & Hagenmuller, P. Structural classification and properties of the layered oxides. *Phys. B* **99,** 81–85 (1980).
24. Meng, Y. S. *et al.* Cation ordering in layered O3 $Li[Ni_xLi_{1/3-2x/3}Mn_{2/3-x/3}]O_2$ ($0 \le x \le 1/2$) compounds. *Chem. Mater.* **17,** 2386–2394 (2005).
25. Mortemard de Boisse, B. *et al.* O3-$Na_xMn_{1/3}Fe_{2/3}O_2$ as a positive electrode materials for Na-ion batteries: structural evolutions and redox mechanisms upon Na^+ (de)intercalation. *J. Mater. Chem. A* **3,** 10976–10989 (2015).
26. Barth, T. F. W. & Posnjak, E. The crystal structure of ilmenite. *Z. Kristallogr.* **88,** 265–270 (1934).
27. Manoharan, S. S. & Sahu, R. K. Evidence for an anomalous redox ionic pair between Ru and Mn in SrRu₀.₅Mn₀.₅O₃: an X-ray absorption spectroscopy approach. *Chem. Commun.* **21,** 3068–3069 (2002).
28. de Groot, F. & Kotani, A. *Core Level Spectroscopy of Solids; Advances in Condensed Matter Science* (CRC Press, 2008).
29. Achkar, A. J. *et al.* Bulk sensitive X-ray absorption spectroscopy free of self-absorption effects. *Phys. Rev. B* **83,** 081106 (R) (2011).

30. Kroll, T. *et al.* X-ray absorption spectroscopy of Na_xCoO_2 layered cobaltates. *Phys. Rev. B* **74**, 115123 (2006).

31. Han, S. W. *et al.* Electronic structure of $RuSr_2EuCu_2O_8$ studied by X-ray absorption and photoemission spectroscopies. *Phys. Rev. B* **85**, 014506 (2012).

32. Pchelkina, Z. V. *et al.* Electronic structure of Li_2RuO_3 studied by LDA and LDA + DMFT calculations and soft X-ray spectroscopy. *Phys. Rev. B* **91**, 115138 (2015).

33. McCalla, E. *et al.* Understanding the roles of anionic redox and oxygen release during electrochemical cycling of lithium-rich layered Li_4FeSbO_6. *J. Am. Chem. Soc.* **137**, 4804–4814 (2015).

34. McCalla, E. *et al.* Visualization of O-O peroxo-like dimers in high-capacity layered oxides for Li-ion batteries. *Science* **350**, 1516–1521 (2015).

35. Sathiya, M. *et al.* Origin of voltage decay in high-capacity layered oxide electrodes. *Nat. Mater.* **14**, 230–238 (2015).

36. Sathiya, M. *et al.* High performance $Li_2Ru_{1-y}Mn_yO_3$ ($0.2 \leq x \leq 0.8$) cathode materials for rechargeable lithium-ion batteries: their understanding. *Chem. Mater.* **25**, 1121–1131 (2013).

37. Saubanère *et al.* The intriguing question of anionic redox in high-energy density cathodes for Li-ion batteries. *Energy Environ. Sci.* **9**, 984–991 (2016).

38. Yu, D. Y. W., Tanagida, K., Kato, Y. & Nakamura, H. Electrochemical activities in Li_2MnO_3. *J. Electrochem. Soc.* **156**, A417–A424 (2009).

39. Koga, H. *et al.* Different oxygen redox participation for bulk and surface: a possible global explanation for the cycling mechanism of $Li_{1.20}Mn_{0.54}Co_{0.13}Ni_{0.13}O_2$. *J. Power Sources* **236**, 250–258 (2013).

40. Tarascon, J. M. *In situ* structural and electrochemical study of $Ni_{1-x}Co_xO_2$ metastable oxides prepared by soft chemistry. *J. Solid State Chem.* **147**, 410–420 (1999).

41. Petříček, V., Dušek, M. & Palatinus, L. Jana2006—the crystallographic computing system: General features. *Z. Kristallogr.* **229**, 345–352 (2014).

42. Monma, K. & Izumi, F. VESTA 3 for Three-dimensional visualization of crystal, volumetric and morphology data. *J. Appl. Cryst.* **44**, 1272–1276 (2011).

43. Kresse, G. & Furthmüller, J. Efficiency of ab-initio total energy calculations for metals and semiconductors using a plane-wave basis set. *Comput. Mat. Sci.* **6**, 15–50 (1996).

44. Klimes, J., Bowler, D. R. & Michaelides, A. Chemical accuracy for the van der waals density functional. *J. Phys. Condens. Matter* **22**, 022201 (2010).

45. Wang, J. C. *et al.* Lattice-tuned magnetism of Ru^{4+} ($4d^4$) ions in single crystals of tshe layered honeycomb ruthenates Li_2RuO_3 and Na_2RuO_3. *Phys. Rev. B* **90**, 161110 (2014).

46. Blaha, P., Schwarz, K., Madsen, G., Kvasnicka, D. & Luitz, J. *WIEN2k, An Augmented Plane Wave + Local Orbitals Program for Calculating Crystal Properties* (Karlheinz Schwarz, Techn. Univ. Wien, Austria, 2001).

Author contributions

M.O. and A.Y. conceived and directed the project. B.M.d.B., G.L. and J.M. synthesized Na_2RuO_3. B.M.d.B., G.L. and J.M. evaluated the electrochemical properties of Na_2RuO_3. B.M.d.B., G.L. and S.N. analysed the XRD patterns of Na_xRuO_3. M.O., H.K. and Y.H. measured and analysed the XAS spectra. J.K. measured and analysed the TEM and electron diffraction micrographs. Y.K. measured and analysed the ^{99}Ru Mössbauer spectra. S.-C.C calculated the oxygen K-edge spectra and the density of states. B.M.d.B., S.N., M.O. and A.Y. wrote the manuscript. All authors commented on the manuscript.

Additional information

Supplementary Information accompanies this paper at http://www.nature.com/naturecommunications

Competing financial interests: The authors declare no competing financial interests.

Reprints and permission information is available online at http://npg.nature.com/reprintsandpermissions/

How to cite this article: Mortemard de Boisse, B. *et al.* Intermediate honeycomb ordering to trigger oxygen redox chemistry in layered battery electrode. *Nat. Commun.* 7:11397 doi: 10.1038/ncomms11397 (2016).